Plastic behavior and failure mechanism of Ti-6Al-4V under quasi-static and dynamic shear loading

Zejian Xu[a,b*], Xiaodong He[a], Hongzhi Hu[a], PJ Tan[b], Yu Liu[a], Fenglei Huang[a*]

[a]State Key Laboratory of Explosion Science and Technology, Beijing Institute of Technology, Beijing 100081, PR China

[b]Department of Mechanical Engineering, University College London, London WC1E 7JE, UK

Abstract

A new kind of double-shear specimen (DSS) is used to study quasi-static and dynamic behaviors of Ti-6Al-4V under simple shear conditions. With different loading techniques, a wide range of shear strain rates are covered from 0.002 s^{-1} to 60000 s^{-1}. The flow stress curves are determined under different conditions. It's observed that the work-hardening effect on the flow stress is weakened gradually with the increasing strain rates. Both the yield stress and the failure initiation stress show an increasing tendency with the strain rates. On the contrary, the failure initiation strain and the fracture strain both decrease with strain rates. From numerical simulation, it's seen that a shear dominated stress/strain state is formed in the shear zone, where the stress triaxiality and the Lode angle parameter basically keep constant for different strain rates. Based on the fracture morphology, it's concluded that with the increasing shear strain rates the failure mechanism changes from a ductile fracture to an ASB dominated process. The macro regularities of the failure properties can be explained well by the different micro-mechanisms.

Keywords: Ti-6Al-4V; dynamic behavior; shear failure; ASB; failure property

1. Introduction

The titanium alloy Ti-6Al-4V is widely used in aerospace, marine, automotive, and other industrial fields due to its high specific strength and stiffness, and good resistance to corrosion and high temperature. During the service period, the structures are usually subjected to both quasi-static and dynamic loading conditions, and hence the mechanical properties and failure mechanism of Ti-6Al-4V are desired over a large range of strain rates. Under high strain rates, especially, it's found that this material is very prone to fail by adiabatic shear banding (Recht, 1964; Liao and Duffy, 1998; Liu et al. 2009), which usually leads to catastrophic damage to the structures. Therefore, the dynamic shear behaviors of Ti-6Al-4V alloys have become the focus of research in recent decades.

Under dynamic loading, the shear deformation (Lee et al., 2006; Peirs et al., 2011a and b) and the evolution of shear localization (Bai et al., 1994; Peirs et al., 2010; Su et al., 2015; Zheng et al., 2016) in Ti-6Al-4V were studied by many researchers in recent years. The failure behaviors of this material have been focused in several researches (Lee et al., 2006; Rittel and Wang, 2008; Zhang et al., 2011; Zheng et al., 2015; Ren et al., 2016; Huang et al., 2018). The effects of microstructures on the mechanical behaviors of Ti-6Al-4V were also studied particularly in some work (Khan et al., 2007; Martinez et al., 2007; Liu et al., 2009; Osovski et al., 2012; Peirs et al., 2013). In addition, constitutive models or failure criterions (Klepaczko, 2000; Chwalik et al., 2003; Seo et al., 2005; Ye et al., 2013) were proposed based on the experimental observations. Among the above-mentioned studies, the most widely used testing method to generate a dynamic loading is the split Hopkinson

* Corresponding author. Tel.: +86 10 68914087
E-mail address: xuzejian@bit.edu.cn (Z. Xu), huangfl@bit.edu.cn (F. Huang)

pressure bar (SHPB) technique. The specimen types include the thin-walled tubular specimen (Bai et al., 1994; Liao and Duffy, 1998; Lee et al., 2006), cylindrical specimen (Zheng et al., 2016; Liu, 2009), shear compression specimen (Rittel and Wang, 2008), hat-shaped specimen (Minnaar and Zhou, 1998; Peirs et al., 2010; Peirs et al., 2013), double-notch specimen (Guo and Li, 2012), in-plane shear specimen (Peirs et al., 2011b) and etc.

Concerning a large domain of strain rates ranging from quasi-static to dynamic conditions, however, systematic investigations on the shear behaviors of Ti-6Al-4V are still rare. The biggest problem is that over a wide range of strain rates, different kinds of specimens are usually required by various loading techniques. As the accuracy of experimental measurement is determined by both the experimental instrument and the specimen geometry, the change of the specimen type may lead to changes in the testing results. Consequently, the comparability and the consistency of the experimental data are difficult to be ensured under different loading methods.

A new kind of double shear specimen (DSS) (Xu et al., 2017; 2018; 2019) was developed recently for studying plastic flow and failure properties of bulk materials under simple shear loading. With the aid of specially designed fixtures, this specimen can be subjected to low and high strain rate testing techniques. In this work, this new specimen is adopted to study the shear behaviors of Ti-6Al-4V under both quasi-static and dynamic conditions. In these tests, the strain rate ranges from 0.002 s^{-1} to 60000 s^{-1}. The effect of strain rate on the failure properties of the material under simple shear condition is studied particularly. The difference in the micro-mechanisms of failure for various strain rates is also investigated based on the examination of the fracture surfaces.

2. Experimental technique

2.1. New DSS specimen

The newly-designed DSS is shown schematically in Fig. 1. It comprises two rectangular shear zones, which have 1 mm in thickness and 4 mm in length. Different strain rates can be generated in the shear zones with different widths *L* of them. In this design, the compression applied on the ends of the specimen can be transformed into local shear in the shear zones. In this work, the shear zone width of the DSS is selected as 0.5 mm for all the tests. This new DSS can be used conveniently under both the SHPB apparatus for dynamic tests and the universal testing machine for quasi-static tests.

The tested material is a commercial Ti-6Al-4V alloy rod. The chemical compositions of this material are given in Table 1. The specimens were removed by wire electro-discharge machining from the alloy rod in the axis direction, and then polished on the surfaces. The microstructures of the material are shown in Fig. 2.

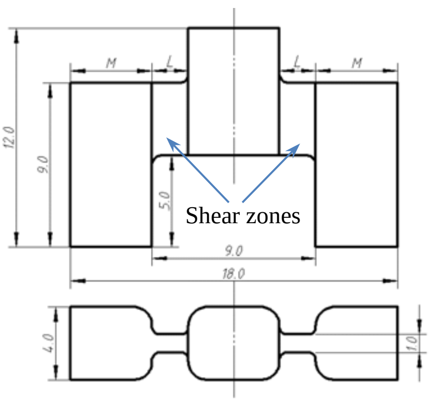

Fig. 1. Schematic diagram of the new DSS specimen.

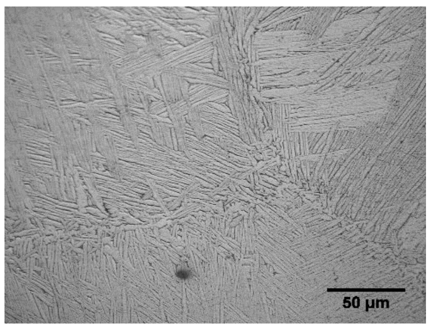

Fig. 2. Microstructure of the Ti-6Al-4V alloy.

2.2. Test methods

The quasi-static tests are performed by the MTS universal testing machine, at two different shear strain rates 0.002 s^{-1} and 2.7 s^{-1}. Fig. 3(a) shows the schematic arrangement of this loading method. In these tests, the transverse displacements of the supporting ends are constrained with a specially designed fixture. In this way, the tensile and bending movements of the shear zones can be prevented. With the force applied on the specimen $F(t)$, the pressing velocity $V(t)$, and the relative displacement of the pressing heads $\Delta L(t)$, in the shear zones the shear strain rate $\dot{\gamma}(t)$, the shear stress $\tau(t)$ and the shear strain $\gamma(t)$ can be determined by

$$\begin{cases} \dot{\gamma}(t) = \dfrac{V(t)}{L} \\ \tau(t) = \dfrac{F(t)}{2A_{sz}} \\ \gamma(t) = \dfrac{\Delta L(t)}{L} \end{cases} \tag{1}$$

where A_{sz} is the sectional area of the shear zone.

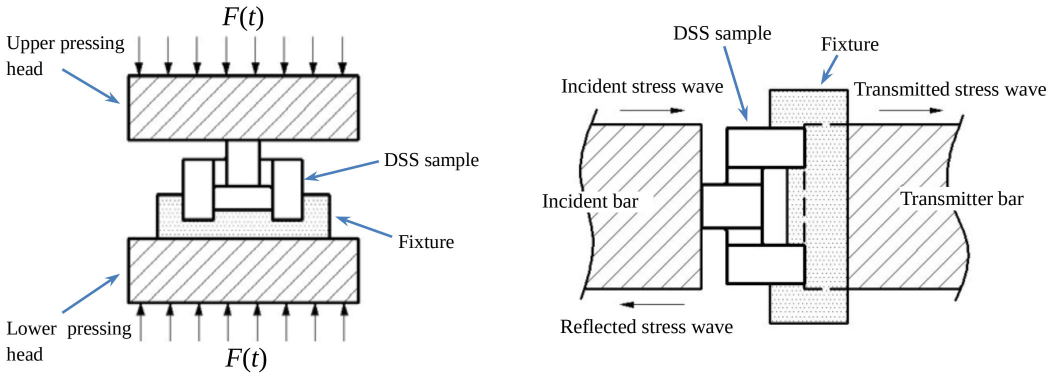

(a) (b)

Fig. 3. Schematic diagram of the quasi-static and dynamic loading methods: (a) the MTS, and (b) the SHPB system.

The dynamic tests were performed using the SHPB technique. The geometric assembly of the dynamic test setup is shown in Fig. 3(b). In these tests, the DSS was put between the incident and transmitter bars. A fixture made of high-strength-steel was used to prevent the transverse displacement of the supporting ends. According to the one-dimensional elastic wave theory, the forces and the displacements at the bar ends can be determined by the strain signals in the bars. Here the incident, reflected, and transmitted strain waves are represented respectively by $\varepsilon_i(t)$, $\varepsilon_r(t)$, and $\varepsilon_t(t)$ in the following equations.

$$\begin{cases} F_{\text{input}} = AE_0\left(\varepsilon_{\text{i}}(t) + \varepsilon_{\text{r}}(t)\right) \\ F_{\text{output}} = AE_1\varepsilon_{\text{t}}(t) \end{cases} \tag{2}$$

$$\begin{cases} U_{\text{input}} = C_0\int_0^t \left(\varepsilon_{\text{i}}(t) - \varepsilon_{\text{r}}(t)\right)\text{d}t \\ U_{\text{output}} = C_1\int_0^t \varepsilon_{\text{t}}(t)\text{d}t \end{cases} \tag{3}$$

where F_{input} and F_{output} are forces, and U_{input} and U_{output} are displacements, at the incident and transmitter bar ends, respectively. E_0 and E_1 are the Young's modulus, and C_0 and C_1 are the longitudinal wave speeds of the incident and transmitter bars, respectively. The shear stress τ, shear strain γ, and shear strain rate $\dot{\gamma}$ in the DSS sample can be determined by the following equations by defining the average force on the specimen $F_{\mathrm{average}}=(F_{\mathrm{input}}+F_{\mathrm{output}})/2$, and the relative displacement of the ends of the specimen $U_{\mathrm{relative}}=U_{\mathrm{input}}-U_{\mathrm{output}}$. Note that in this method γ is actually a global shear strain, which represents the deformation situation of the whole sample.

$$\begin{cases} \tau(t)=\dfrac{F_{\mathrm{average}}}{2A_{\mathrm{sz}}} \\ \gamma(t)=\dfrac{U_{\mathrm{relative}}}{L} \\ \dot{\gamma}(t)=\dfrac{C_0\left(\varepsilon_{\mathrm{i}}(t)-\varepsilon_{\mathrm{r}}(t)\right)-C_1\varepsilon_{\mathrm{t}}(t)}{L} \end{cases} \quad (4)$$

3. Results and discussion

3.1. Experimental results

The shear stress-shear strain curves obtained at 0.002 s^{-1} and 2.7 s^{-1} are given in Fig. 4. It's observed that under the quasi-static conditions, the shear stress-shear strain curves show an obvious work-hardening effect. After yielding of the material, the flow stress increases smoothly to the largest value, and then it decreases slightly before the specimen fractures suddenly. As no necking takes place in the shear tests, the decrease of the flow stress generally results from the formation of microcracks at the shear zones. Therefore, the highest point of the flow stress curve can be determined as the initiation of the failure process of the material. With the increasing shear strain, the flow stress drops a little firstly due to steady extension of the microcracks, and then the cracks coalesce and propagate very quickly, resulting in a sudden drop of the flow stress. Comparing these two strain rates, the shear stress-shear strain curves at 2.7 s^{-1} are slightly higher than those at 0.002 s^{-1}. It means that the flow stress of the material shows a strain rate effect. For example, with the strain rate rising from 0.002 s^{-1} to 2.7 s^{-1}, the average value of the yield stress is elevated from 452 MPa to 522 MPa, while the flow stress at the fracture initiation point increases from 608 MPa to 674 MPa.

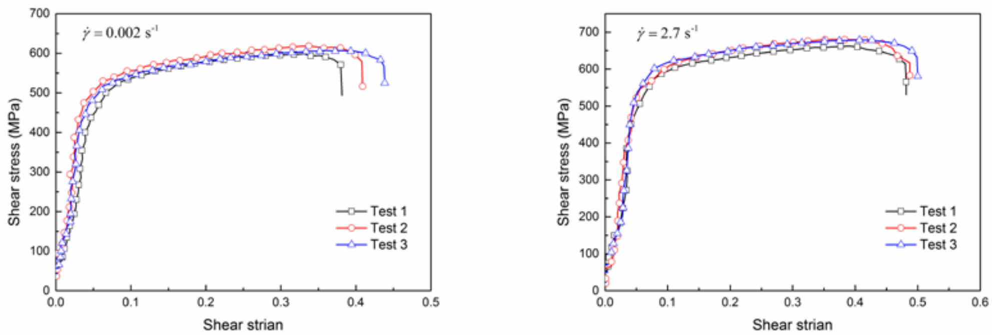

(a) (b)

Fig. 4. Shear stress-shear strain curves with quasi-static loading: (a) 0.002 s^{-1}, and (b) 2.7 s^{-1}.

Under dynamic loading, the typical stress waves measured by the SHPB technique are given in Fig. 5. The shear strain rate of this test is 11700 s^{-1}. It's seen that the duration of the transmitted signal is obviously shorter than that of the incident signal. It indicates that the specimen was broken under the impact loading. After the breaking of the specimen, the subsequent incident stress wave was totally reflected back into the incident bar. Therefore, in the reflected stress wave the signal decreases first, and then at the breaking point it increases back to the same level as the incident signal. According to Eq. (4), the shear strain and shear stress curves with time are determined in Fig. 6. The shear stress-shear strain curve is shown in Fig. 7.

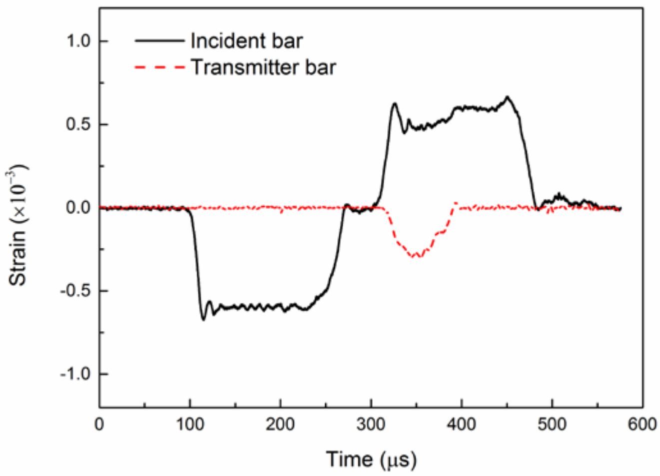

Fig. 5. Typical stress waves determined by the SHPB technique at 11700 s^{-1}.

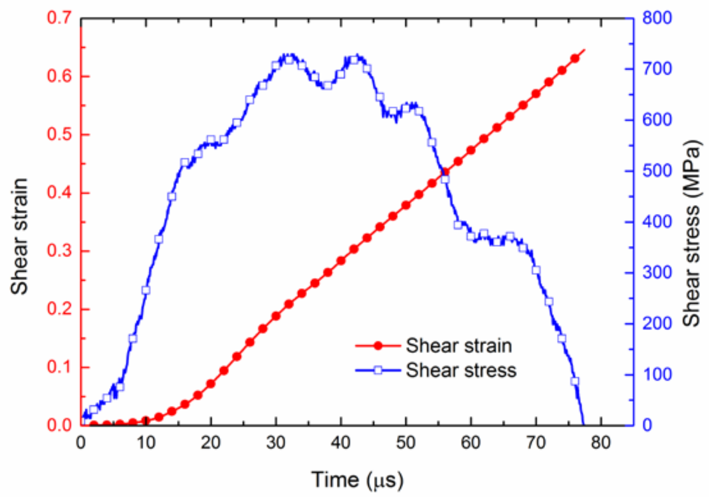

Fig. 6. Shear stress and shear strain curves with time at 11700 s^{-1}.

In Fig. 7, the material yields at point A, then the flow stress increases with shear strain to point B, showing clearly a work-hardening effect. After that, the flow stress exhibits some oscillations due to the stress wave effect, but it keeps relatively a steady level to point C. After that, the flow stress shows a fast decreasing tendency until it becomes zero at point D, which indicates the total fracture of the specimen. Therefore, this whole deformation process may be divided into three stages: First, from the beginning of the loading to point A is the elastic stage. Second, the section from point

A to point C represents a steady plastic deformation stage. In this stage the material deforms plastically but the failure does not take place yet. The last stage represents the failure process of the material, which is between points C and D. Hence point C indicates the initiation of the failure process in the specimen. Similarly, in other dynamic tests we also choose the turning point of the stress curve, at which the flow stress begins to descend quickly to zero, as the failure initiation stress.

In these SHPB tests, the deformation process of the DSS sample was monitored by a high speed camera, with the capture rate of 80000 fps. Seven lines with equal intervals of 0.5 mm were drawn across the shear zone of the specimen. The deformation process of the shear zone from 0 μs to 75 μs is shown from the shear stress-shear strain curve in Fig. 7. It's clear that the determined global shear strain by this method is in a good accordance with the local average shear strain obtained by the camera-based measurement. Hence the measured stress/strain results are valid by the present testing method. From the photos, it can also be observed that the shear zones of the specimen didn't break completely until the shear stress went down to zero. It means that during the failure process, the capacity of the material to support load is deteriorated continually, which is different from the failure mode in the quasi-static tests. In the quasi-static tests, there is a steady growth period of the crack after it is initiated, and then the shear zone is fractured very abruptly. Under dynamic loading, in contrast, the material will fail continually once the failure process is initiated. In this test, for example, the flow stress goes down from 628 MPa at point C to zero at point D, with a total time of about 26 μs.

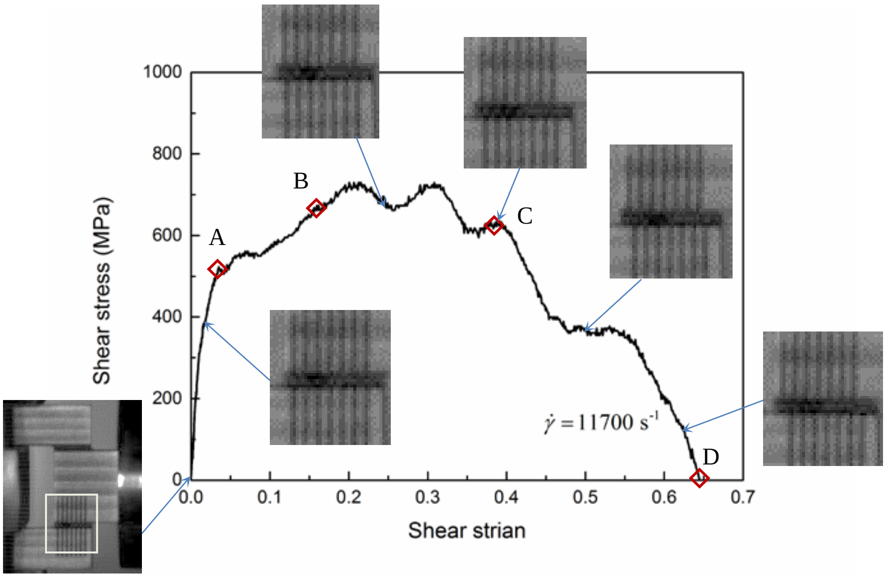

Fig. 7. Shear stress-shear strain curve and the deformation process of the specimen at 11700 s^{-1}.

The flow stress curves obtained under dynamic loadings from 4000 s^{-1} to 60000 s^{-1} are given together in Fig. 8. For comparison, the shear stress curves tested at 0.002 s^{-1} and 2.7 s^{-1}, as well as the stress-strain curve of a uni-axial tensile test at 0.001 s^{-1}, are also exhibited in the same plot. The tensile curve is obviously higher than the shear results. For the shear tests, the effect of the strain rate can be clearly seen from the flow stress curves. For example, the work-hardening effect is obvious for quasi-static conditions, but under dynamic loadings, the flow stress will keep steady (e.g. 4000 s^{-1}) or even goes down to some extent (e.g. 8000 s^{-1}). This is induced by the adiabatic temperature rise during the plastic deformation. When the strain rate increases to 20000 s^{-1}, the flow stress shows basically a decreasing tendency from the yielding point. At 21000 s^{-1}, the plastic flow stage becomes very short because the failure process is initiated at the shear strain of 0.27. For even higher strain rates, no obvious plastic flow stage can be observed. Instead, the shear stresses rise from the beginning of the loading to a peak point (fracture stress) and then they decline very quickly to zero. It indicates that at higher strain rates the specimens failed in a very early stage of the loading process. It's interesting to note that with the increase of strain rates, the failure process also tends to be finished earlier gradually. For example, in Fig. 8 the shear strains at which the shear stresses decline to zero also present clearly a decreasing tendency. Under different strain rates, distinct fractographic features can be observed for this material. Some typical microstructures for different strain rates are given together with the flow stress curves. It indicates that with the increase of the strain rates, the failure of the material is controlled by different mechanisms. Detailed analysis on the failure characteristics of the material will be given in Section 4. The original and loaded samples at different strain rates are shown in Fig. 9.

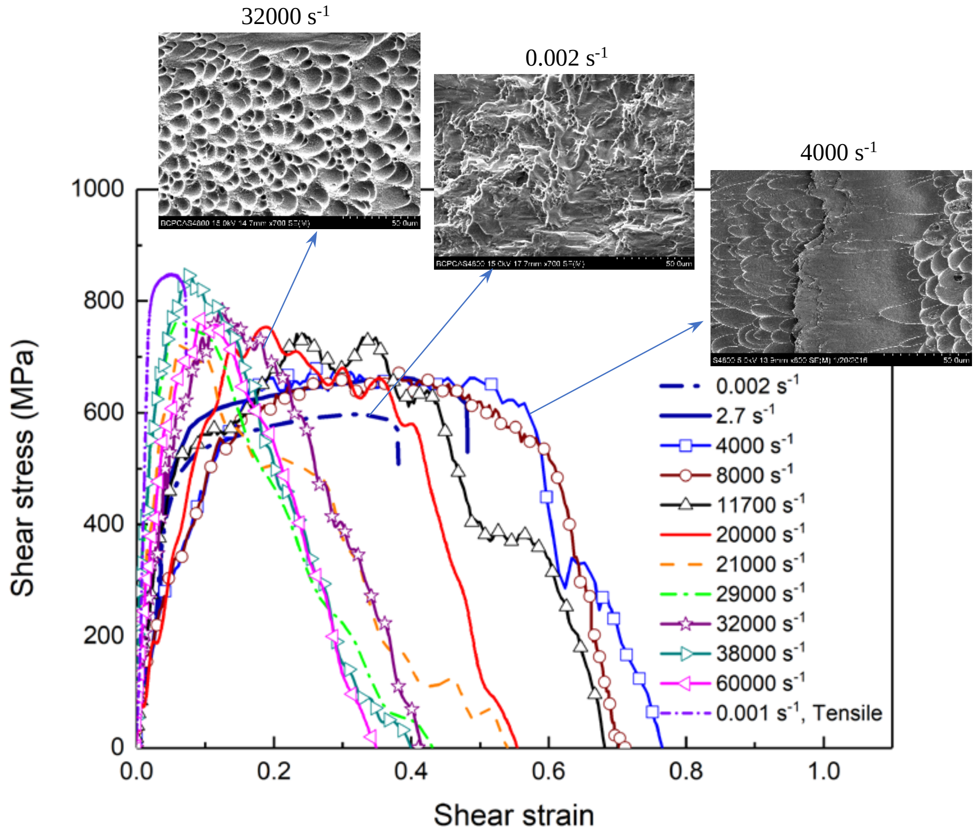

Fig. 8. Shear stress-shear strain curves for different strain rates under quasi-static and dynamic conditions. (The stress-strain curve in a tensile test at 0.001 s^{-1} is also given. Typical microstructures in the failure surfaces under 0.002 s^{-1}, 4000 s^{-1}, and 32000 s^{-1} are shown.)

Fig. 9. The original and loaded DSS samples under different strain rates: (a) original, (b) 0.002 s^{-1}, (c) 4000 s^{-1}, and (d) 35000 s^{-1}.

To examine the effect of the strain rate on the failure behaviors of the material, the yield stress and the failure initiation stress are given together in Fig. 10 as functions of the strain rate. It's seen that the yield stress shows a slightly increasing trend at first. The increase of the yield stress with the strain rates is even more obvious under dynamic conditions. The failure initiation stress is generally larger than the yield stress for each strain rate, but they have very similar tendencies with the increase of strain rate. For higher strain rates (above 21000 s^{-1}), the specimens were generally fractured at the peak point of the curves (Fig. 8). Therefore, the yield stresses are only determined for tests under 21000 s^{-1}. The fracture stresses for these tests are also given in Fig. 10. It can be seen that the fracture stresses are evidently larger than the failure initiation stresses of the lower strain rates. The results show that the strain rate has a significant effect on the yielding and failure stresses of the material.

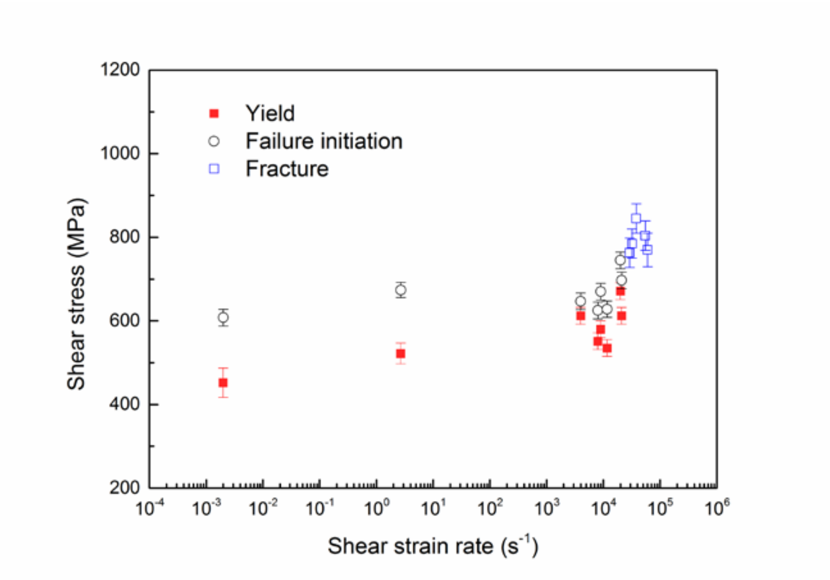

Fig. 10. The strain rate effect on the yield stress, the failure initiation stress, and the fracture stress.

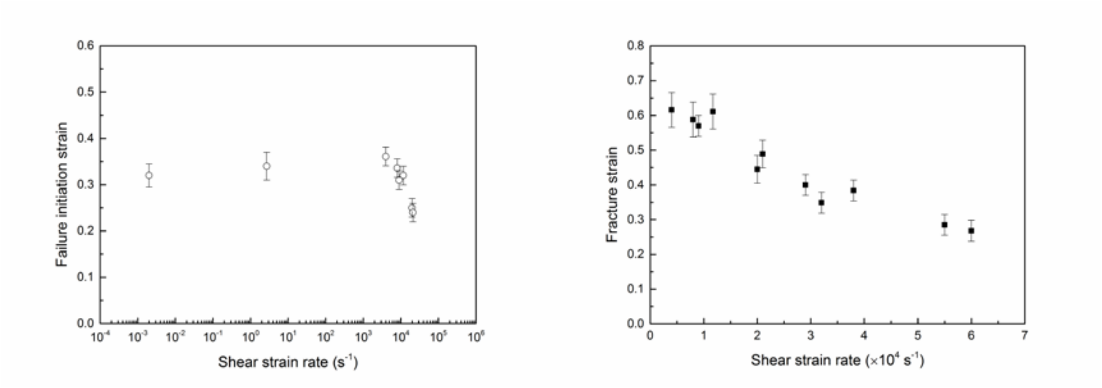

(a) (b)

Fig. 11. The strain rate effect on (a) the yield and the failure initiation strains, and (b) the fracture strain.

Subtracting the elastic portion from the deformation, the failure initiation strains under quasi-static and dynamic loading conditions are plotted against shear strain rate in Fig. 11(a). It's seen that with the strain rate increasing from 0.002 s^{-1} to 2.7 s^{-1}, the failure initiation strain changes very slightly. Under dynamic loading, however, the failure initiation strain shows a rapid decline with the increase of the strain rate. Note that only the results with plastic deformation stages are given in this plot. It implies that the failure process may be controlled by different mechanisms under quasi-static and dynamic conditions. In order to further examine the strain rate effect on the failure property of the material under high strain rates, the fracture strain, at which the specimen completely broke, is shown against the strain rate in Fig. 11(b). It's clear that the fracture strain also decreases with the increase of the strain rates. It means that the failure process will be initiated at an earlier stage for higher strain rates, and meanwhile the material tends to fail more easily. To get an in-depth understanding to the mechanisms of the failure behaviors, the stress/strain states of the material should be analyzed. Meanwhile, the micro-structural evolution at different strain rates need to be examined.

3.2. Stress states in the shear zone

To obtain the stress state in the shear zones under dynamic conditions, the loading process is simulated using the finite element (FE) program ABAQUS/Explicit. During the 3D simulation, full-size models of the NDSS samples and the Hopkinson bars are used. The material parameters used in the models are given in Table 2. The bars and the fixture are treated as elastic bodies. As for the DSS sample, the Johnson-Cook (JC) material model determined by Seo et al. (2005) is used to represent the thermoplastic behavior of the material. The von Mises flow stress σ is expressed in the JC model as

$$\sigma = \left(A + B\varepsilon^n\right)\left(1 + C\ln\dot{\varepsilon}^*\right)\left(1 - T^{*m}\right) \tag{5}$$

Here ε is the equivalent plastic strain; $\dot{\varepsilon}^* = \dot{\varepsilon}/\dot{\varepsilon}_0$ is the dimensionless plastic strain rate for $\dot{\varepsilon}_0 = 1$ s^{-1}; $T^* = \left(T - T_{\mathrm{r}}\right)/\left(T_{\mathrm{m}} - T_{\mathrm{r}}\right)$ is the homologous temperature, where T is the absolute temperature, T_{m} (=1941 K) is the melting temperature of the material, and T_{r} (= 298 K) is the reference temperature. The material constants are given in Table 3.

Table 2 Material parameters used in the FEA

Part	Material	Density (g/mm^3)	E (GPa)	μ	Thermal conductivity (W/(m·K))	Specific heat (J/(kg·K))
Specimen	Ti-6Al-4V	4.43	114	0.33	6.7	470
Incident bar	18Ni	8.0	190	0.3	-	-
Transmitter bar	7075 Al alloy	2.7	70	0.3	-	-

Table 3 Material constants for the JC model (Seo et al., 2005)

A(MPa)	B(MPa)	n	C	m
997.9	653.1	0.0198	0.45	0.7

The contact properties of the sample/bar and sample/fixture interfaces are "Hard" contact. The frictional forces on the interfaces are neglected. The incident stress wave is applied as pressure on the end of the incident bar. The 8-node linear brick, reduced integration elements (C3D8R) were used in the bars. The 10-node modified thermally coupled second-order tetrahedron elements (C3D10MT) were used in the sample to simulate the adiabatic temperature rise in the shear zones. The fraction of the plastic work converted into heat is set as 0.9. The initial temperature in the sample is 298 K. The elements were refined in the shear zones so that the stress/strain conditions can be modeled accurately.

At 4000 s^{-1}, the time curves of the average stress and strain components for the whole shear zone are shown in Fig. 12. The coordinate system is given in Fig. 13 along with the central plane of the DSS. In Fig. 12, the shear zone is dominated by the shearing components σ_{13} and ε_{13} for the whole loading process. As the specimen actually broke at about 129 μs, after that moment the curves should be neglected. In Fig. 12(a), σ_{13} increases quickly from the beginning to above 650 MPa, and after that it keeps steady. The other components are evidently lower than σ_{13}. In Fig. 12(b), ε_{13} increases almost linearly to the failure point. At this moment ε_{13} is about 0.14, while the other components are all much less than ε_{13}. For example, ε_{11} and ε_{33} are -0.013 and -0.0007, respectively. It indicates that the stress state of the material in the shear zone can be regarded as plane shear. Therefore, a shear dominated stress/strain condition can be realized by this new kind of DSS under dynamic loading.

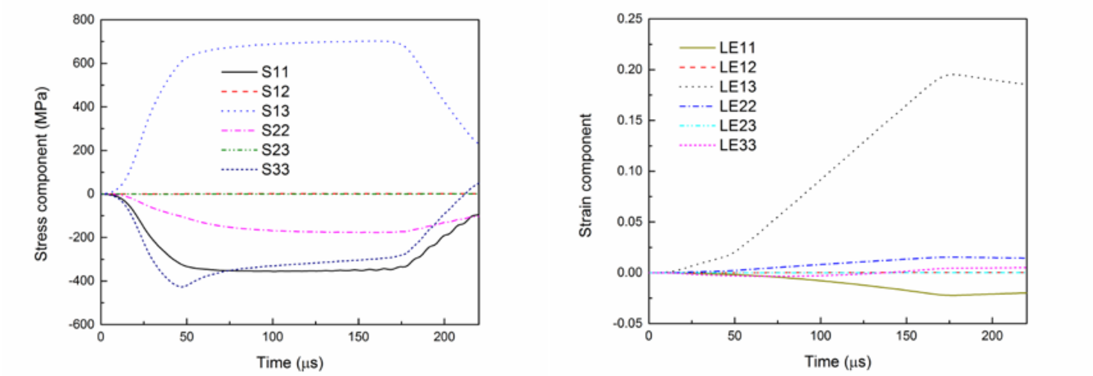

(a) (b)

Fig. 12. Distribution of the stress and strain in the shear zone of the DSS sample at the strain rate of 4000 s^{-1}: (a) stress components and (b) strain components.

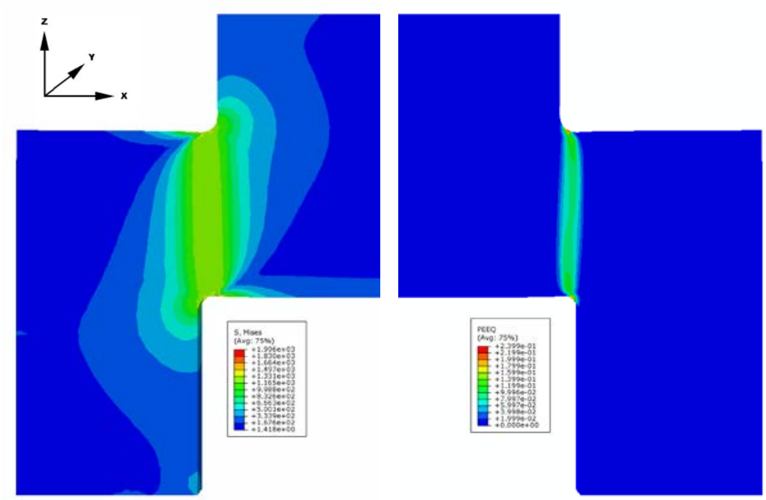

(a) (b)

Fig. 13. Distribution of the (a) equivalent stress and (b) equivalent strain in the central plane of the DSS sample at the failure time.

At the failure moment, the distribution of the equivalent stress and plastic strain is shown in Fig. 13 for the central plane of the specimen. In Fig. 13(a), a large stress gradient appears in the loading and supporting blocks of the specimen. In contrast, the stress is quite uniform inside the shear zone. It's clear that in Fig. 13(b), the distribution of the plastic strain in the central part of the shear zone is also uniform. No plastic deformation is formed in the loading or supporting ends of the specimen.

Larger plastic stain is generated at the corners of the shear zone due to stress/strain concentration. It explains why the DSS specimens generally broke along the diagonal of the shear zones.

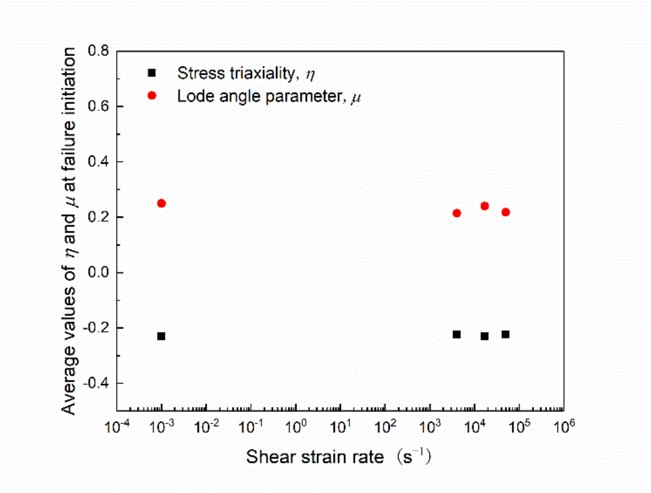

Fig. 14. The strain rate effect on the average values of η and μ for the whole shear zone at the failure initiation time.

To characterize the stress state in the shear zone, the stress triaxiality η, and the Lode angle parameter μ are usually used. They represent the effects of the hydrostatic stress and the third deviatoric stress invariant, respectively. η and μ are usually defined as follows:

$$\eta = \frac{\sqrt{2}(\sigma_1 + \sigma_2 + \sigma_3)}{3\sqrt{(\sigma_1 - \sigma_2)^2 + (\sigma_2 - \sigma_3)^2 + (\sigma_3 - \sigma_1)^2}} \tag{6}$$

$$\mu = \frac{2\sigma_2 - \sigma_1 - \sigma_3}{\sigma_1 - \sigma_3} \tag{7}$$

where σ_1, σ_2, and σ_3 are the three principle stresses with $\sigma_1 \geqslant \sigma_2 \geqslant \sigma_3$. At the failure moment, the average values of these parameters in the whole shear zone are shown in Fig. 14, for both quasi-static and dynamic conditions. It's seen that the values of η and μ change very little for the different strain rates. They basically keep constant at an average level of -0.226 for η, and 0.231for μ, respectively. It again shows that a shear-dominated stress state exists in the material. Considering the stress components along the coordinate axes, the material in the shear zone is actually in a simple shear deformation condition.

The comparison between the measured and the simulated results for both the shear stress-shear strain curves and the equivalent stress-equivalent strain curves at 4000 s^{-1} are given in Fig. 15. It's seen that the calculated shear stress curve is very close to the test result, except that the simulation data shows a rising tendency. The simulated equivalent stress curve is obviously higher than the test result. The difference between the simulated and tested flow stress curves may result from the inconsistency between the constitutive model (Seo et al., 2005) and the mechanical property of the present material. It should also be noted that in the determination of the JC model, the stress state effect on the material is not considered. For a better description of the plastic behavior of the material, the actual stress/strain state must be considered in the tests and in the determination of the constitutive models (Xu et al., 2019). This problem will be further studied in our future work.

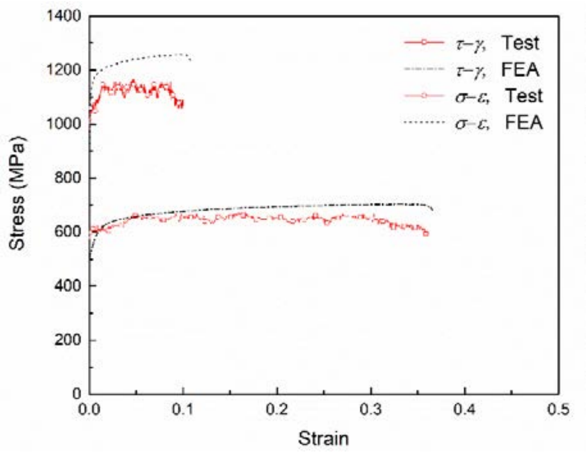

Fig. 15. Comparison between the experimental and the simulated stress-strain curves for a test at the strain rate of 4000 s^{-1}.

4. Failure analysis

The typical fracture morphology under quasi-static conditions is shown in Figs. 16 and 17. Under 0.002 s^{-1}, for example, a lot of tearing ridges with sharp tips and layered structures are observed in the breaking surface, Fig. 16(a). From a higher magnification of the same SEM image, shallow dimples are clearly seen below these tearing edges, Fig. 16(b). It indicates that the material fails in a typical ductile fracture mode. Different from a tensile deformation, under simple shear the growth of voids is constrained. With negative stress triaxiality actually, the voids are flattened out to micro-cracks. With the increasing deformation, the micro-cracks interact and coalesce with the neighboring ones, forming sharp tearing ridges and shallow dimples. At 2.7 s^{-1}, the layered structures are even more obvious, Fig. 17(a). At the edges of different layers, bright and zigzag steps are formed by the jointing of the tearing ridges. Smooth and flat regions are also present at some layers. These regions are actually fracture surfaces extended from micro-cracks. Magnified images at the steps (Fig. 17(b)) show that along with the bright ridges, there also exist a large amount of small dimples. Flat fracture surfaces can also be observed in the same image. These features show that under quasi-static loading this alloy mainly fails in a ductile mode, with mixed patterns of dimples and tearing ridges.

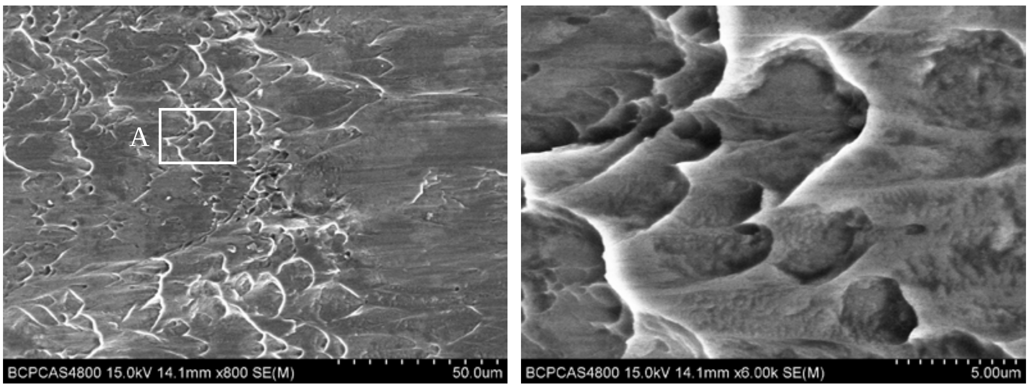

(a) (b)

Fig. 16. Fracture morphology of the material at 0.002 s^{-1}: (a) tearing ridges with sharp tips, and (b) dimples below the tearing ridges from magnification of section A.

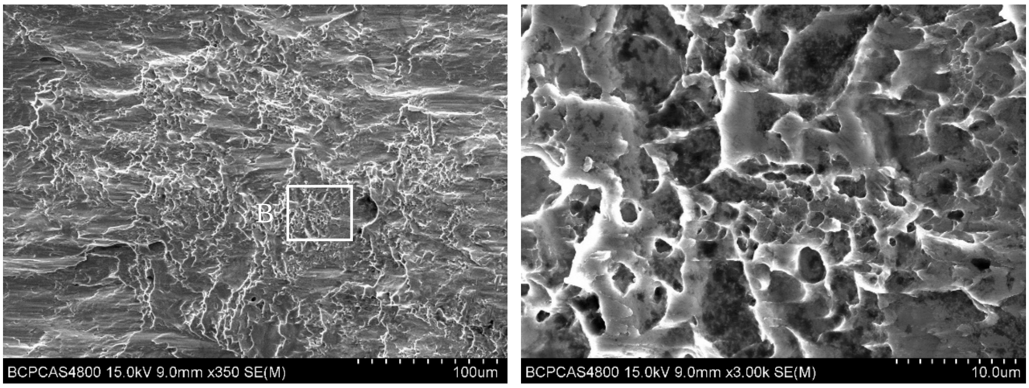

(a) (b)

Fig. 17. Fracture morphology of the material at 2.7 s^{-1}: (a) layered structures and steps, and (b) dimples from magnification of section B.

Under dynamic loading, the fracture surfaces show totally different patterns from quasi-static conditions. At 8000 s^{-1}, for example, many parabolic patterns present in the failure surface in Fig. 18(a). In Fig. 18(b), the amplified image shows that these patterns are actually severely stretched dimples. It means that under high strain rates the adiabatic temperature rise plays an important role in the failure process. When the temperature approaches the melting point during the fast deformation, the material tends to flow within the shear plane in the direction of the shear stress. In this way the plastic deformation is localized in a thin layer and adiabatic shear band (ASB) is generated. In this process, the dimples are elongated severely and they take the shape of parabolic patterns. For higher strain rates, ASBs form more easily because higher temperatures can be reached for a certain plastic deformation with less heat dissipation. It may explain why the failure initiation strain decreases quickly with strain rates under dynamic condition in Fig. 11(a). This phenomenon agrees well with the results of Sargent and Ashby (1983) for their study of the same material.

In Fig. 18(a), some smooth areas appear in the fracture surface. It's seen in Fig. 18(c) that these areas are actually smeared surfaces, resulting from rubbing between the fracture surfaces in the shear bands. At the smooth surfaces, largely elongated dimples can be found. Flow characteristics and river patterns that were formed by molten metal are obvious at these locations.

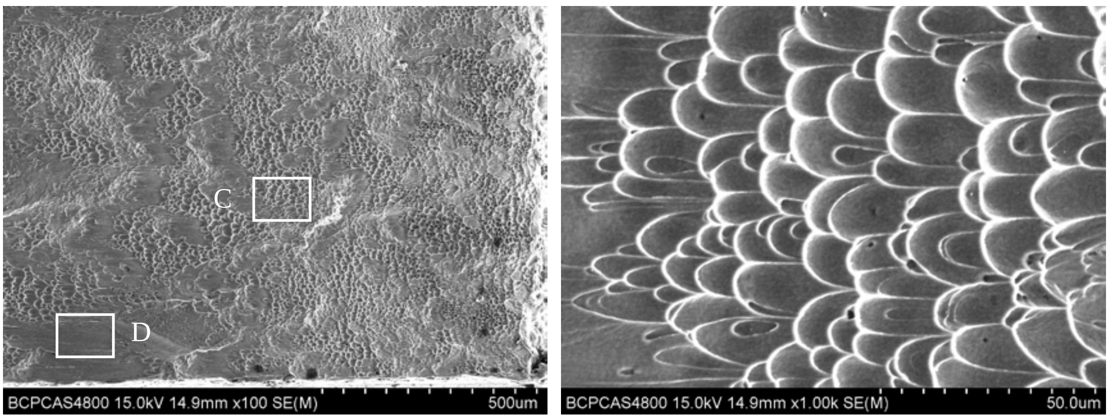

(a) (b)

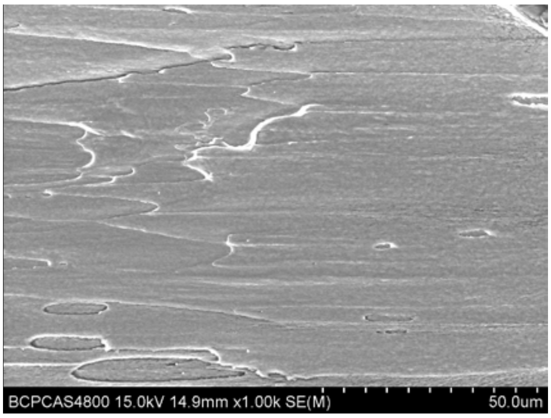

(c)

Fig. 18. Fracture morphology of the material at 8000 s^{-1}: (a) parabolic patterns and smooth areas at the fracture surface, (b) severely stretched dimples from magnification of section C, and (c) smeared areas from magnification of section D.

When the strain rate is further elevated, e.g. 32000 s^{-1}, much more smooth flow patterns are present along with the dimples at the failure surfaces, Fig. 19(a). It indicates that more ASBs are generated in the fracture surface along with the elongation of dimples. In Fig. 19(b) it can be observed that a large amount of oval-shaped dimples present at the failure surface. Very small voids exist within the larger elliptical dimples (Fig. 19(c)). However, the dimples are less elongated comparing with 8000 s^{-1}. It means that the shear plane separates at a much earlier stage of the shear deformation. At this moment, many small voids haven’t grown into larger dimples yet, and only slight elongation can be seen in the voids and dimples in the shear direction. Therefore, the fracture strain has a decreasing tendency with the increase of strain rates in Fig. 11(b).

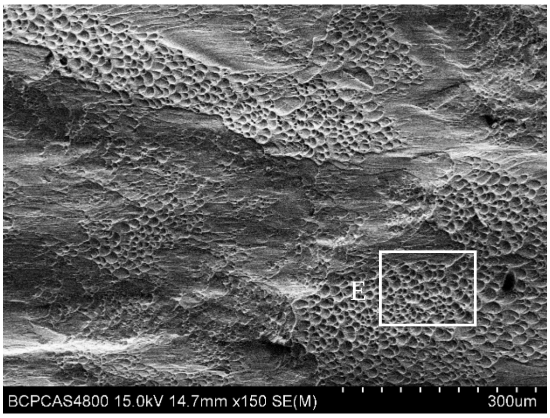

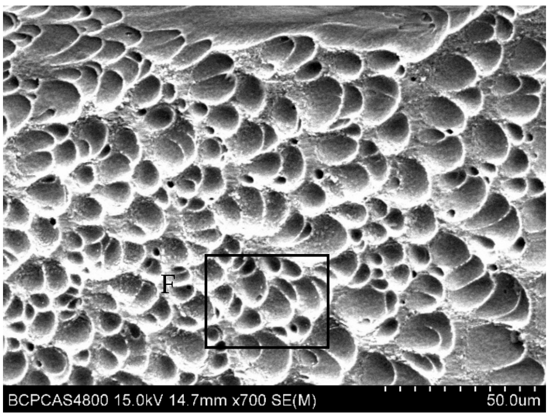

(a) (b)

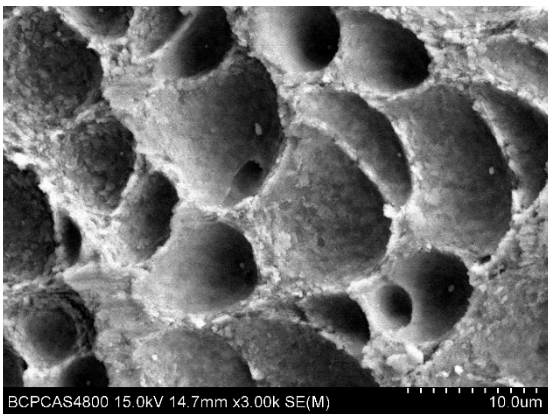

(c)

Fig. 19. Fracture morphology of the material at 32000 s^{-1}: (a) smooth flow patterns and deformed dimples at the fracture surface, (b) oval-shaped dimples from magnification of section E, and (c) small voids within the elliptical dimples from magnification of section F.

Based on the above analyses, it can be concluded that for different shear strain rates the failure process of the material is controlled by different mechanisms. Under quasi-static loading, the material mainly fails in the mode of ductile fracture. The typical patterns are dimples and tearing ridges. Smooth and flat fracture regions can also be observed at the fracture surfaces. Under dynamic conditions, on the contrary, thermal softening and ASB plays the dominant roles in the failure process. Severely elongated dimples generally present in the failure surface. The failure initiation point corresponds to the occurrence of the localization of deformation at the beginning of adiabatic shear banding. Therefore, the failure initiation strain goes down with the increase of the strain rate due to an easier formation of ASB. At even higher strain rates, more ASBs show up in the fracture surface, and the shear plane separates more easily at an earlier stage of the shear deformation. Consequently, the fracture strain declines with the increasing strain rates. Very small voids and subdimples are distributed in the failure surfaces for such cases.

5. Conclusion

A new kind of DSS is used to study quasi-static and dynamic failure behaviors of Ti-6Al-4V under simple shear conditions. With different loading techniques, a large strain-rate range is covered from 0.002 s^{-1} to 60000 s^{-1} with the same type of DSS. Failure properties are determined, and the fracture morphology is examined to study the micro-mechanisms of the failure process under different conditions. The conclusions are summarized as following.

1) Under quasi-static loading, the flow stress of the material shows clearly a work-hardening effect. Under dynamic loading, this work-hardening effect is not obvious. At 20000 s^{-1}, the flow stress begins to show a decreasing tendency from the early stage of the plastic deformation.
2) At high strain rates, the flow stage of the material is shortened due to an earlier initiation of the failure process. Above 29000 s^{-1}, only a peak shows up in the flow stress curves, indicating the failure of the material at an early stage of the loading process.
3) Both the yield stress and the failure initiation stress show an increasing tendency with the increasing of strain rates. On the contrary, the failure initiation strain and fracture strain both show a decreasing trend with strain rates. It means that the strain rate effect is obvious on the yielding and failure processes of the material.
4) From numerical simulation, it's seen that the shear zone is under a shear dominated stress state. The stress/strain fields are quite uniform in the center of the shear zone. For different strain rates, η and μ basically keep constant in the shear zone at average levels of -0.226 and 0.231, respectively.
5) Based on fracture morphology, it's seen that the failure process of the material is controlled by different mechanisms for different strain rates. It changes from ductile fracture at quasi-static conditions, to an ASB dominated process at high strain rates. The macro regularities of the failure properties can be explained well through the analysis of the micro-mechanisms of the failure process.

Acknowledgements

The authors gratefully acknowledge the financial support from National Natural Science Foundation of China (No. 11772062, 11302030). This work is also partially supported by the State Key Laboratory of Explosion Science and Technology (YBKT17-03, 19-08) and the NSFC for innovative research groups (11521062).

References

Bai Y., Xue Q., Xu Y., Shen L.. Characteristics and microstructure in the evolution of shear localization in Ti-6A1-4V alloy. Mechanics of Materials, 1994 , 17 (2-3) :155-164

Chwalik P., Klepaczko J.R., Rusinek A.. Impact shear-numerical analyses of ASB evolution and failure for Ti-6AI-4V alloy. Journal de Physique IV, 2003, 110 :257-262

Guo, Y., Li, Y., 2012. A novel approach to testing the dynamic shear response of Ti-6Al-4V. Acta Mechanica Solida Sinica. 25(3), 299–311.

Huang, J., Guo, Y., Qin, D., Zhou, Z., Li, D., Li, Y., 2018. Influence of stress triaxiality on the failure behavior of Ti-6Al-4V alloy under a broad range of strain rates. Theoretical and Applied Fracture Mechanics. 97: 48-61.

Khan A.S., Kazmi R., Farrokh B., Zupan M.. Effect of oxygen content and microstructure on the thermo-mechanical response of three Ti-6Al-4V alloys: Experiments and modeling over a wide range of strain-rates and temperatures. International Journal of Plasticity 23 (2007) 1105–1125

Klepaczko J.R.. Behavior of Ti-6Al-4V alloy at high strain rates, shear testing up to 6 x 10E4 1/s and failure criterion. J. Phys. IV France 10 (2000) Pr9-191-Pr9-196

Klepaczko, J.R., 1998. Remarks on impact shearing. Journal of the Mechanics and Physics of Solids. 46(10), 2139-2153.

Lee W.S., Lin C.F., Huang S.Z.. Effect of temperature and strain rate on the shear properties of Ti–6Al–4V alloy. Proc. IMechE Vol. 220 Part C: J. Mechanical Engineering Science. 2006 , 220 (2) :127-136

Liao S., Duffy J.. Adiabatic shear bands in a Ti-6Al-4V titanium alloy. J. Mech. Phys. Solids, 46 (1998) 2201-2231

Liu X., Tan C., Zhang J., et al., 2009. Influence of microstructure and strain rate on adiabatic shearing behavior in Ti-6Al-4V alloys. Mater Sci Eng A 501: 30-36

Liu X., Tan C., J Zhang., Wang F., Cai H.. Correlation of adiabatic shearing behavior with fracture in Ti-6Al-4V alloys with different microstructures. International Journal of Impact Engineering 36 (2009) 1143-1149

Martinez F., Murr L.E., Ramirez A., Lopez M.I., Gaytan S.M.. Dynamic deformation and adiabatic shear microstructures associated with ballistic plug formation and fracture in Ti-6Al-4V targets. Materials Science and Engineering A 454-455 (2007) 581-589

Minnaar K., Zhou M.. An analysis of the dynamic shear failure resistance of structural metals. Journal of the Mechanics and Physics of Solids, Volume 46, Issue 10, 1 October 1998, Pages 2155-2170

Osovski S., Rittel D., Landau P., Venkert A.. Microstructural effects on adiabatic shear band formation. Scripta Materiallia 66 (2012) 9-12

Peirs J., Tirry W., Amin-Ahmadi B., Coghe F., Verleysen P., Rabet L., Schryvers D., Degrieck J.. Microstructure of adiabatic shear bands in Ti6Al4V. Materials Characterization 75(2013)79-92

Peirs J., Verleysen P., Degrieck J., Coghe F., 2010. The use of hat-shaped specimens to study the high strain rate shear behaviour of Ti–6Al–4V. International Journal of Impact Engineering 37 (2010) 703-714

Peirs J., Verleysen P., Degrieck J., 2011a. Experimental Study of the High Strain Rate Shear Behaviour of Ti6Al4V. Applied Mechanics & Materials , 2011 , 82 :130-135

Peirs J., Verleysen P., Paepegem W. V., Degrieck J.. Determining the stress–strain behaviour at large strains from high strain rate tensile and shear experiments. International Journal of Impact Engineering 38 (2011b) 406-415

Recht R.F.,1964. Catastrophic thermoplastic shear. J Appl Mech 31(2): 189-193

Ren G., Guo Z., Fan C., Tang T., Hu H.. Dynamic shear fracture of an explosively-driven metal cylindrical shell. International

Journal of Impact Engineering 95 (2016) 35-39

Rittel, D., Lee, S., Ravichandran, G., 2002. A Shear-compression specimen for large strain testing. Exp. Mech. 42, 58-64.

Rittel D., Wang Z.. Thermo-mechanical aspects of adiabatic shear failure of AM50 and Ti6Al4V alloys. Mechanics of Materials 40(2008) 629-635.

Sargent P.M., Ashby M.F., 1983. Cambridge Univ. Engng. Dept. Report No. CUED/C/MATS/TR.98.

Seo S, Min O, Yang H. Constitutive equation for Ti–6Al–4V at high temperatures measured using the SHPB technique. Int. J. Impact. Eng, 2005, 31(6):735-754

Su G., Gong X., Li Y., Guo Y., Suo T.. Shear behavior of TC4 alloy under dynamic loading. Explosion and Shock Waves 35(4) (2015) 527-535

Xu, Z., Ding, X., Zhang, W., Huang, F., 2017. A novel method in dynamic shear testing of bulk materials using the traditional SHPB technique. Int. J. Impact Eng. 101: 90–104.

Xu, Z., Liu, Y., Sun, Z., Hu, H., Huang, F., 2018. On shear failure behaviors of an armor steel over a large range of strain rates. Int. J. Impact Eng. 118: 24–38.

Ye G.G., Xue S.F., Jiang M.Q., Tong X.H., Dai L.H.. Modeling periodic adiabatic shear band evolution during high speed machining Ti-6Al-4V alloy. International Journal of Plasticity 40 (2013) 39–55

Zhang J., Tan C., Ren Y., Yu X., Ma H., Wang F., Cai H.. Adiabatic shear frature in Ti-6Al-4V alloy. Trans. Nonferrous Met. Soc. China 21(2011) 2396-2401.

Zheng C., Wang F., Cheng X., J Liu., Liu T., Zhu Z., Yang K., Peng M., Jin D.. Captureing of the propagating processes of adiabatic shear band in Ti-6Al-4V alloys under dynamic compression. Materials Science & Engineering A658 (2016) 60-67

Zheng C., Wang F., Cheng X., et al. Failure mechanisms in ballistic performance of Ti-6Al-4V targets having equiaxed and lamellar microstructures. International Journal of Impact Engineering 85 (2015) 161-169